Department of Applied Physics

Integrating Normal-Metal Components into the Framework of Circuit Quantum Electrodynamics

Philip Jones

Aalto University

DOCTORAL DISSERTATIONS

Aalto University publication series
DOCTORAL DISSERTATIONS 104/2013

Integrating Normal-Metal Components into the Framework of Circuit Quantum Electrodynamics

Philip Jones

A doctoral dissertation completed for the degree of Doctor of Science in Technology to be defended, with the permission of the Aalto University School of Science, at a public examination held at the lecture hall K216 (Mechanical Engineering Building 1) on the 14th of June 2013 at 12:00.

Aalto University
School of Science
Department of Applied Physics
Quantum Computing and Devices

Supervising professor
Prof. Risto Nieminen

Thesis advisor
Doc. Mikko Möttönen

Preliminary examiners
Prof. Kalle-Antti Suominen, University of Turku, Finland
Prof. Ilari Maasilta, University of Jyväskylä, Finland

Opponent
A/Prof. Andrea Morello, University of New South Wales, Australia

Aalto University publication series
DOCTORAL DISSERTATIONS 104/2013

ISBN 978-952-60-5224-3 (printed)
ISBN 978-952-60-5225-0 (pdf)
ISSN-L 1799-4934
ISSN 1799-4934 (printed)
ISSN 1799-4942 (pdf)
http://urn.fi/URN:ISBN:978-952-60-5225-0

Unigrafia Oy
Helsinki 2013

Finland

441 697
Printed matter

Aalto University

Abstract

Aalto University, P.O. Box 11000, FI-00076 Aalto www.aalto.fi

Author
Philip Jones

Name of the doctoral dissertation
Integrating Normal-Metal Components into
the Framework of Circuit Quantum Electrodynamics

Publisher School of Science

Unit Department of Applied Physics

Series Aalto University publication series DOCTORAL DISSERTATIONS 104/2013

Field of research Engineering Physics, Theoretical and Computational Physics

Manuscript submitted 15 April 2013 **Date of the defence** 14 June 2013

Permission to publish granted (date) 24 May 2013 **Language** English

☐ **Monograph** ☒ **Article dissertation (summary + original articles)**

Abstract

Superconducting quantum bits are one of the leading frontrunners in the race to build a solid-state quantum computer. In circuit quantum electrodynamics (cQED), electronic quantum circuits, playing the role of quantum bits, qubits, are placed into superconducting cavities with incredibly weak dissipation. The resulting system exhibits both photon and qubit characteristics, and it is possible to perform complex operations by driving the system with microwaves. Progress has been rapid, with vast improvements in cavities, qubits, and in controlling the interaction between the two. As a result, the first simple quantum algorithms to utilize this architecture have recently been implemented.

At the same time, there have been significant developments in improving our understanding of the heat flow in nanoelectronics. In particular the development of tunnel junctions has reached such a level, that it is now possible to control and measure the temperature of small metal islands with high precision. Such techniques have enabled the first observations of quantum-limited heat conduction through the photonic modes of a circuit.

This thesis introduces some of the benefits that come with the unification of these two fields. Theoretical models for experiments in a superconducting cavity are presented, with heat conduction due to individual cavity photons discussed in detail, along with a novel method to vary the lifetime of a qubit over many orders of magnitude. The realisation of these experiments would be the first steps on the road to integrating normal-metal components with cQED.

Keywords Circuit Quantum Electrodynamics, Photonic Heat Transport, Remote Heating and Cooling, Superconducting Quantum Bits

ISBN (printed) 978-952-60-5224-3 **ISBN (pdf)** 978-952-60-5225-0

ISSN-L 1799-4934 **ISSN (printed)** 1799-4934 **ISSN (pdf)** 1799-4942

Location of publisher Espoo **Location of printing** Helsinki **Year** 2013

Pages 98 **urn** http://urn.fi/URN:ISBN:978-952-60-5225-0

Preface

The research presented here was undertaken between 2010 and 2013 in the Department of Applied Physics at Aalto University School of Science. During this time, I have been working in the Quantum Computing and Devices (QCD) group, which is a member of the Centre of Excellence in Computational Nanoscience (COMP).

I would like to thank my supervisor, Aalto Distinguished Professor Risto Nieminen, for the chance to be a part of COMP, with all of the additional benefits that this entails. Special thanks must of course go to my instructor Adjunct Professor Mikko Möttönen, from whom most of these ideas stem, for giving me the opportunity to come to Finland, and most of all for the huge effort he has put in during my final push for graduation. I am grateful to Paolo, Kuan, Juha, Harri, Joonas, Ville, Russell, Tuomo, and all of the other members of the QCD group for putting up with me during this time. Undoubtedly however, it has been Jukka, Emmi, and Pekko who have endured far more than most. I would especially like to single out Jukka who, in addition to feeding me almost half a herd of reindeer, found the time to help me much more than I think he realised. I am also very thankful to Juha for deviating from his preferred topic, and working so hard to help me with my final paper. Finally, I am indebted to the financial support of the National Graduate School in Materials Physics.

Helsinki, May 24, 2013,

Philip Jones

Contents

Preface i

Contents iii

List of Publications v

Author's Contribution vii

1. Introduction 1

2. Quantum Computing with circuit QED 3

2.1 Superconducting Qubits 3

2.2 SQUIDs in a Coplanar Waveguide Cavity 4

3. Photonic Heat Conduction in Nanoelectronics 7

3.1 Observation of Quantum-Limited Heat Conduction due to Photons 7

3.2 Tunnel Junction Thermometry 9

4. Cavity with a Position-Dependent Inductance 11

4.1 Quantum Lagrangian Analysis 12

4.2 Classical Matrix Analysis 15

5. Single-Photon Heat Transfer in a Cavity 19

5.1 Calculation of the Photonic Heat Power in a Cavity 19

5.2 Remote Heating and Cooling of a Dissipative Cavity Element 22

6. Tunable Environment for Superconducting Qubits 25

6.1 Distributed-Element Cavity Model 25

6.2 Lumped-Element Resonator System 29

7. Summary 35

Bibliography **37**

Publications **41**

Errata **43**

List of Publications

This thesis consists of an overview and of the following publications which are referred to in the text by their Roman numerals.

I Philip Jones, Jukka Huhtamäki, Kuan Yen Tan, and Mikko Möttönen. Single-photon heat conduction in electrical circuits. *Physical Review B*, **85**, 075413, February 2012.

II Philip Jones, Jukka Huhtamäki, Matti Partanen, Kuan Yen Tan, and Mikko Möttönen. Tunable single-photon heat conduction in electrical circuits. *Physical Review B*, **86**, 035313, May 2012.

III Philip Jones, Jukka Huhtamäki, Juha Salmilehto, Kuan Yen Tan, and Mikko Möttönen. Tunable electromagnetic environment for superconducting quantum bits. *Submitted to Scientific Reports*, April 2013.

IV Philip Jones, Juha Salmilehto, and Mikko Möttönen. Highly controllable qubit-bath coupling based on a sequence of resonators. *Submitted to Journal of Low Temperature Physics*, April 2013.

Author's Contribution

Publication I: "Single-photon heat conduction in electrical circuits"

The author performed all of the published analytical and numerical calculations and wrote the manuscript.

Publication II: "Tunable single-photon heat conduction in electrical circuits"

The author performed all of the published analytical and numerical calculations and wrote the manuscript.

Publication III: "Tunable electromagnetic environment for superconducting quantum bits"

The author performed all of the published analytical and numerical calculations and wrote the manuscript.

Publication IV: "Highly controllable qubit-bath coupling based on a sequence of resonators"

The author performed some of the published analytical calculations, all of the numerical calculations, and contributed very significantly to the writing of the manuscript.

1. Introduction

In 1905, the *annus mirabilis*, Albert Einstein published his four seminal works and triggered an immensely productive period of activity in quantum mechanics. Several decades later, towards the end of this golden age in physics, Claude Shannon would introduce his new information theory [1], a seemingly unrelated, but no less important work. Einstein and his contemporaries had revolutionised the fundamental framework of physics, but the impact of Shannon's ideas has ultimately proven to be even more far-reaching, providing the necessary foundations for the transformation to our modern mass-communication society.

The effect of information theory on physics has been no less significant, indeed looking at physics from the perspective of information has led physicists down a very fruitful path, a journey which would eventually cause them to question the nature of reality itself [2–4]. In the years following the publication of Shannon's masterpiece, it was gradually realised that information is intimately connected to the physical world, and it is equally as fundamental as energy or entropy [5, 6]. In particular, since a computer is nothing more than a device which stores and acts on information, any computation is a physical process[1] [8].

The implications of this point become truly fascinating when the worlds of Shannon and Einstein are combined. If information is physical, then its behaviour must be governed by the laws of physics, which are ultimately believed to be quantum mechanical. Applying quantum principles to computing suggests the possibility of creating novel computers which can be vastly more powerful than their classical counterparts [9–11]. This huge speed up is fundamentally a consequence of utilizing the two lynchpins of the quantum mechanical world. The first of these, superposition, provides

[1]The reverse is also true, any physical process may be considered a computation. Indeed as Seth Lloyd has noted [7], the universe is itself a computer, a computer that happens to compute its own evolution.

the possibility for a quantum system to simultaneously exist in multiple states, à la Schrödinger's infamous cat. The second critical element is entanglement, Einstein's "spooky action at a distance", which allows the physical properties of quantum objects to remain correlated even when separated across galactic distances.

Since any two-level system can in principle perform the role of the quantum bit, qubit, many candidates have been proposed. Natural qubits such as spin-1/2 particles or photons have many attractive features and are the subject of intense study [12–14]. In practice building a real quantum computer is an extremely difficult engineering challenge, and currently no one system has all of the necessary attributes required, namely [15]

1. The ability to reset the qubit to a simple state.
2. A method to operate on, and make precise measurements of qubits.
3. Scalability of the system to a large number of qubits[2].
4. A set of one qubit operations and at least one non-trivial two qubit gate.
5. Coherence times far greater than the time needed to apply one gate.

The problem is essentially that these factors can be, to a large extent, mutually exclusive. Photons, for example, do not couple very strongly to the environment which makes them resilient to noise. On the other hand, they do not couple strongly to other photons either, making qubit-qubit interactions difficult. The work in this thesis culminates with a method to improve the initialization of superconducting qubits without harming their coherence times (Publications III and IV). We reach this goal via several important milestones, most notably the theoretical prediction of heat conduction due to single photons in a cavity (Publications I and II).

The overview is organised as follows. Chapter 2 gives a brief introduction to circuit quantum electrodynamics. Some of the latest experiments in photonic heat conduction are reviewed in Chapter 3. Chapter 4 introduces the theoretical basis required for both our studies on single-photon heat conduction, the subject of Chapter 5, and on a tunable environment for superconducting qubits, which is presented in Chapter 6. Finally Chapter 7 concludes this thesis with a summary of the main results.

[2]Small toy quantum computers with up to 14 qubits have successfully implemented Shor's Factoring Algorithm [16, 17]. This algorithm is important for encryption reasons, but will require $\sim 10^{4-5}$ qubits to tackle practical problems [18–20]. Nevertheless, even a quantum computer consisting of ~ 50 qubits is likely to have some interesting uses [21, 22].

2. Quantum Computing with circuit QED

This chapter gives some background on superconducting quantum bits in microwave cavities, a field that provides much of the motivation for our work and helps to place it in context.

2.1 Superconducting Qubits

A long term goal of this research is to provide new tools for superconducting qubits. These qubits encompass several different kinds of superconducting circuits that can be engineered to have atom-like properties. Unlike intrinsic two-level systems, these artificial atoms are coherent over macroscopic dimensions. Macroscopic quantum coherence in electronics was first predicted in 1980 [23], but it would be two decades before experimental techniques reached the necessary level of sophistication to allow for definitive observation [24]. The phenomenon is perhaps best exemplified by large superconducting rings, systems of $\sim 10^{10}$ electrons in which a macroscopic current can simultaneously flow clockwise and anticlockwise [25, 26].

The large number of degrees of freedom involved permits strong coupling to other circuits, making multi-qubit gates possible. Even better, and unlike real atoms, these circuits can be designed to have specific (and often tunable) parameters. Being solid-state devices, construction of these artificial atoms is also appealing from a practical point of view, allowing well-developed fabrication techniques to be employed. However, by exploiting orders of magnitude more degrees of freedom to gain increased qubit-qubit coupling, we must inevitably contend with a correspondingly stronger qubit-environment interaction [27, 28]. Experimentalists have risen to the challenge of extending decoherence times and, though there is still some way to go, qubit lifetimes have improved by a factor of 10^4 or

so, in comparison to the first pioneering superconducting qubits [29]. This enhancement has been achieved through a combination of reducing both the sensitivity of the qubit to noise and the noise itself [30–32]. In this thesis the precise choice of qubit is not crucial, we care only that viable qubits exist. The specific details of the various different types of superconducting qubits are therefore not discussed here; these can be found, for example, in Refs. [33, 34].

Instead, our interest lies with the architecture. The qubits are typically coupled to a superconducting coplanar waveguide transmission line resonator. These transmission lines operate in the microwave regime, where they effectively act as one dimensional Fabry-Perot cavities. The cavities can be manufactured with extremely high quality-factors $Q \geq 10^{6-7}$ [35], meaning that the photonic excitations in the resonator can, classically speaking, travel a distance of several kilometres before exiting the cavity. This setup, in which a single photon mode is coupled to a qubit in a superconducting resonator, is referred to as circuit quantum electrodynamics (cQED) [36–41]. The cavity-qubit coupling mixes the states of the two systems producing new eigenstates that have both photonic and qubit character with an anharmonic energy level spacing. By coupling several qubits to the cavity, the resonator can be used to mediate an interaction between spatially separated qubits [42–44]. Entanglement of one or more qubits can now be routinely achieved [45–47], and implementation of the first algorithms has recently been reported [48, 49]. Though driven primarily by quantum computing, cQED has proved to be a stellar test bed for fundamental quantum mechanics. From the manipulation and generation of single-photons [50–52], to the production of several exotic quantum states [53, 54], the control exerted by experimentalists over this domain has reached a high level of sophistication.

In this thesis, we will demonstrate that, in theory, we can insert normal metal components into the cavity in a useful manner. In Publication III and IV we do exactly this, with the proposal for a new method to initialize superconducting qubits.

2.2 SQUIDs in a Coplanar Waveguide Cavity

The Josephson junction is the key component of superconducting circuits, providing the non-linearity needed for interesting physics without introducing dissipation which would cause decoherence. Such a junction occurs

at a weak link between two superconductors, through which a supercurrent, i.e., Cooper Pairs, may flow in the absence of an applied voltage. If two of these junctions are combined in parallel to from a loop, we obtain a **s**uperconducting **qu**antum **i**nterference **d**evice (SQUID). These SQUIDs are regularly employed in a variety of low temperature experiments and are important building blocks for superconducting qubits. If the instantaneous current through the SQUID if much lower than its critical current, then the non-linear response of the SQUID, i.e., the dependence of the inductance on the instantaneous current, can be neglected [55]. In this case, it is reasonable to approximate a SQUID as an inductor, whose inductance is a function of the magnetic flux penetrating the loop Φ [56],

$$L_J = \frac{\hbar}{4eI_c} \frac{1}{|\cos\left(\frac{\pi\Phi}{\Phi_0}\right)|}, \tag{2.1}$$

where the magnetic flux quantum is denoted by $\Phi_0 = \frac{h}{2e}$, and I_c is the critical current of each junction. In modelling the SQUID as an inductor, we also disregard its junction capacitance C_J, which may be assumed to have only a small effect on the total conductance, in the regime of small signal frequency $\omega \ll \frac{1}{\sqrt{L_J C_J}}$.

By constructing the central resonator entirely or partially with SQUIDs[1], it is possible to tune the resonance frequency *in situ* by varying the flux through the SQUIDs. Such techniques provide a useful means, for example, to quickly detune the resonator from the qubit[2] [55, 56]. One stunning achievement enabled by this approach, has been the observation of photons created by rapidly changing the effective length of the transmission line, a phenomenon referred to as the dynamical Casimir effect [59, 60].

[1] Alternatively the SQUID may be placed at the end of the line to tune the boundary conditions

[2] Recently a new type of qubit has been designed which provides a tunable coupling to the resonator, independent of the cavity or qubit frequency [57, 58].

3. Photonic Heat Conduction in Nanoelectronics

For further background, we review recent experiments on the observation of photonic heat conduction, as well as work on the temperature control of small metal islands via tunnel junctions.

3.1 Observation of Quantum-Limited Heat Conduction due to Photons

Quantum computation is far from the only interesting consequence of applying quantum mechanical principles to information exchange. A second notable effect is revealed by the presence of the thermal conductance quantum, $g_0 = \frac{\pi^2 k_B^2 T}{3h}$, an upper bound on the thermal conductance of a one-dimensional quantum channel at a temperature T [61, 62]. This effect becomes important when the coherence length of the heat carriers becomes comparable to the size of the sample, as can be the case in low-temperature nanosystems. It is precisely because this limit to the maximum thermal power is derived from an information-theoretic standpoint that it can be applied so generally, completely independent of the materials used, or the specific details of the circuit design. It also holds regardless of the nature of the heat carriers, be they electrons [63], phonons [64], or indeed photons [65].

To see this fundamental limitation in practice, typically requires the low temperatures only found in dilution refrigerators. Even at these temperatures, it can still be somewhat unusual to see photons mentioned in discussions of heat conduction. However, this photonic pathway can be a significant thermal relaxation mechanism in ultra-low temperature nanoelectronics. Consider, for example, the circuit shown in Fig. 3.1, in which two metallic islands, of average temperature T, are connected by superconducting leads. Unlike electrons, Cooper pairs do not transport energy

by diffusion and therefore no such conventional electronic thermal conduction is possible through the leads between the islands. The heat power transferred out of each island as a result of the coupling of the electrons in the metal with the phonons in the lattice is, typically, proportional to T^5 [66]. In comparison, the photonic heat flux between the two islands in such a circuit has (depending on the precise details of the circuit) a T^2 dependence [67]. Therefore, at least in some nanosystems, there exists a regime in which the competing conduction channels are frozen out, and photon heat conduction is dominant. The crossover to this new regime usually occurs at a temperature somewhere in the region of $100 - 200$ mK.

Such a circuit is precisely what was fabricated in the experiment of Meschke *et al* [65]. In this case, the heat conduction is a consequence of the thermal agitation of the electrons in the metal, this motion produces random voltage fluctuations across the islands, which are transmitted through the electromagnetic modes of the circuit, and have the two-sided Johnson-Nyquist power spectrum

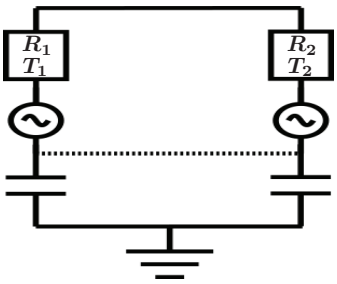

Figure 3.1. Equivalent circuit of a connected island structure. The impedance, and hence the power transmitted, is dependent on the presence of the dashed lead, which forms a loop geometry. Adapted from Timofeev *et al* [67].

$$S_V(\omega, T) = \frac{2R\hbar\omega}{1 - \exp(\frac{-\hbar\omega}{k_B T})}, \qquad (3.1)$$

where T is the temperature of the resistor, and negative frequencies are allowed [68]. By utilizing a SQUID to vary the impedance of the circuit, they were able to tune the photonic heat conduction between the islands. The power reaches its maximum for an impedance matched circuit, connected in a ring geometry, with a value measured to be in good agreement with the thermal quantum [65].

A more recent experiment [67], adapted this setup and successfully demonstrated remote photonic refrigeration. By lowering the temperature of one island they were able to observe the cooling of a second island at a separation of about 50 μm. This distance is much smaller than the wavelength of the thermal photons[1] and the lumped element model shown in Fig. 3.1 is therefore valid[2]. Thus the power transfer may be modelled

[1] At 100 mK, $\lambda_{\text{th}} = hc/k_B T \approx 5$ cm.

[2] This was also the case in Ref. [65]

using the semiclassical equation [66]

$$P_\gamma = \int_0^\infty \frac{d\omega}{2\pi} \frac{4R_1R_2\hbar\omega}{|Z_t(\omega)|^2} \left(\frac{1}{\exp\left(\frac{\hbar\omega}{k_BT_2}\right)-1} - \frac{1}{\exp\left(\frac{\hbar\omega}{k_BT_1}\right)-1} \right), \tag{3.2}$$

which gives the photonic power through a circuit of total impedance $Z_t(\omega)$, including islands 1 and 2, which have resistances R_1, R_2 and temperatures T_1, T_2, respectively.

These studies have approached the subject from the point of view of understanding how the electromagnetic environment affects ultra-sensitive experiments and devices. As electronic devices become increasingly miniaturised, knowledge of the heat transport on the chip becomes increasingly important. The additional photon channel can couple isolated components. This feature may be a hindrance when attempting to maintain components at distinct quasiequilibrium temperatures, or prove beneficial, for example, in refrigeration [69, 70]. The focus of this thesis is slightly different, and aims to provide a tunable environment for components placed into a superconducting cavity, a theme found throughout. In a cavity, the photons have a well defined frequency and we are therefore able to associate the heat conduction with individual microwave photons. This subject is explored in detail in Publications I and II.

3.2 Tunnel Junction Thermometry

There are two tools which are absolutely crucial for all of the work presented in this thesis. If we place a normal-metal island into a cavity, it is essential that we have, firstly, a practical method to measure the temperature of the island, and secondly, the ability to control the temperature of the island over a range of several hundred millikelvins. In fact, both of these can be accomplished using the same underlying principle [71, 72]. The basic idea is rather elegant, and is explained below.

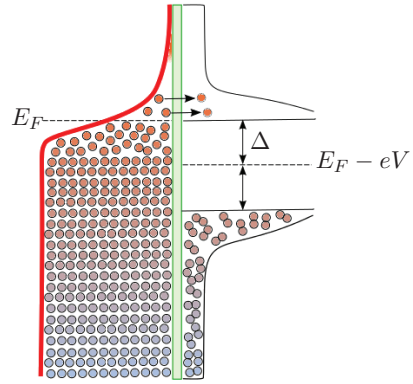

Figure 3.2. In NIS thermometry a bias is applied over the normal metal, shifting the Fermi level of the metal relative to the superconducting gap. Adapted from Muhonen *et al* [71].

Fundamentally, the cooling of an electron reservoir is equivalent to a narrowing of its Fermi distribution around the Fermi

energy, E_F. In NIS cooling, hot electrons (with $E > E_F$) are removed from the reservoir (see Fig. 3.2), while cold electrons ($E < E_F$) may also be added. This is accomplished by taking advantage of the superconducting density of states $N_S(E)$, which has an energy gap forbidding electronic excitations in the region $E_F \pm \Delta$. In a low-temperature normal-metal–insulator–superconductor (NIS) junction at equilibrium, this gap prevents hot electrons from tunnelling out of the normal metal into the superconductor. By applying a suitable bias to the normal metal we can shift the Fermi energy of the metal relative to the superconducting gap, increasing or reducing the rate at which electrons tunnel out of the reservoir. In this way, the temperature of the normal-metal may be varied considerably.

The accessible electron temperature range depends on the initial bath temperature, as well as the BCS gap in the superconductor, Δ. For aluminium, the most common superconducting material, and assuming realistic bath temperatures, this technique allows a normal-metal island to be cooled down to around 100 mK. Below this temperature however, cooling becomes significantly more challenging [73, 74]. In suspended devices, temperatures of 42 mK have been achieved in islands for which the electron temperature at zero-bias is 100 mK [75].

The NIS thermometer works on a very similar principle. When a small, constant current bias is maintained across the junction, a measurement of the voltage allows the temperature of the normal metal to be inferred. These NIS techniques are especially attractive as they operate directly on the chip, which can simplify the experimental setup significantly. The use of NIS junctions for thermometry and temperature control are assumed throughout this thesis, the power introduced to the islands by the NIS probes is considered explicitly only in Publication II.

4. Cavity with a Position-Dependent Inductance

Exciting photons in the transmission line induces voltage and current waves which travel along the length of the line. In the microwave regime, photon wavelengths are typically comparable to the size of the waveguides; the voltage and current can therefore differ considerably over the length of the device, rendering a lumped LC oscillator model incomplete. Nevertheless, as shown in Fig. 4.1, the transmission line can be divided into many smaller sections, each of which does have a lumped element representation [76].

In this chapter, we describe two possible methods to calculate the mode profiles in the resonator. We first employ the Lagrangian formalism to acquire an analytic result for the voltage and current operators. The second technique describes the system as a classical eigenvalue problem, permitting the inclusion of dissipative elements in a straightforward manner.

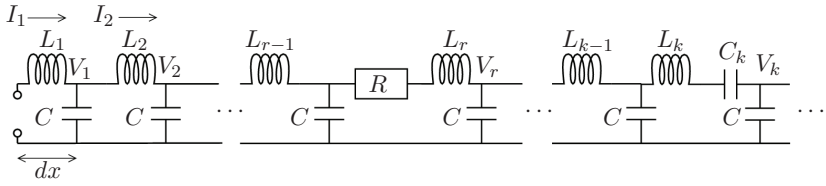

Figure 4.1. Equivalent circuit of a transmission line. We can model a transmission line by considering an infinitely long sequence of L and C elements. The values of these elements are chosen in order to match the inductance per unit length ℓ, of the central conducting strip $L_i = \ell\, dx$, and the capacitance per unit length c, between the line and ground plane $C = c\, dx$. In this figure the transmission line has been modified by the introduction of a resistor at node r and a capacitor at node k. In addition, one may include SQUIDs by adding an inductor of inductance $L + L_J(\phi)$ at the appropriate nodes.

4.1 Quantum Lagrangian Analysis

In the quantum description, we model the resonator using the language of the harmonic oscillator, defining creation and annihilation operators for the photon number states. Applying the Lagrangian formalism to Fig. 4.1, the voltage and current operators of a standard cavity[1] are found to be [36],

$$\hat{V}_{\text{cav}} = \sum_{k=1}^{\infty} \sqrt{\frac{\hbar\omega_k}{Lc}} \cos\left(k\pi x/L\right) [\hat{a}_k(t) + \hat{a}_k^\dagger(t)], \tag{4.1}$$

$$\hat{I}_{\text{cav}} = \sum_{k=1}^{\infty} i\sqrt{\frac{L\hbar c\omega_k^3}{k^2\pi^2}} \sin\left(k\pi x/L\right) [\hat{a}_k(t) - \hat{a}_k^\dagger(t)], \tag{4.2}$$

where L is the length of the cavity, with ℓ and c the inductance and capacitance per unit length, respectively. We denote the bosonic annihilation and creation operators of the jth cavity mode by $\hat{a}_j(t)$ and $\hat{a}_j^\dagger(t)$. The jth mode has an angular frequency ω_j, which for this standard cavity takes a value $\omega_j = j\pi/(L\sqrt{\ell c})$.

We now extend the Lagrangian method to a more general case, which allows for a capacitor of capacitance C_c at x_c, and a position dependent inductance per unit length $\ell(x)$ of the form

$$\ell(x) = \begin{cases} \ell_L, & 0 \leq x \leq x_c, \\ \ell_R, & x_c < x \leq L. \end{cases} \tag{4.3}$$

Our starting point is the discrete model of the circuit shown in Fig. 4.1. In the continuum limit $dx \to 0$, the integral of the charge density stored in the capacitors of Fig. 4.1, can be defined as $\Theta(x',t) = \int_0^{x'} q(x,t)\,dx$, and the Lagrangian may be written in terms of Θ as

$$\mathcal{L} = \int_0^L \left[\frac{\ell(x)}{2} \left(\frac{\partial\Theta}{\partial t}\right)^2 - \frac{1}{2c}\left(\frac{\partial\Theta}{\partial x}\right)^2 - \frac{\Theta^2}{2C_c}\delta(x - x_c) \right] dx. \tag{4.4}$$

We assume that the cumulative charge may be separated into the form $\Theta(x,t) = \sum_j X_j(x)T_j(t)$, to arrive at the Euler-Lagrange equations

$$\frac{1}{c\ell(x)X_j(x)}\frac{\partial^2 X_j(x)}{\partial x^2} - \frac{1}{C_c\ell(x)}\delta(x - x_c) = -\omega_j^2, \tag{4.5}$$

$$\frac{1}{T_j(t)}\frac{\partial^2 T_j(t)}{\partial t^2} = -\omega_j^2. \tag{4.6}$$

We observe that in the time domain each mode has simple harmonic behaviour, while the spatial variation has the same form as the time-

[1] A cavity which can be modelled using only a homogenous inductance and capacitance per unit length.

independent Schrödinger equation of a particle in a delta function potential. The latter can be solved with a plane wave Ansatz. Taking the boundary conditions $X_j(0) = X_j(L) = 0$, and applying continuity at x_c, the solutions are found to be

$$X_j(x) = \begin{cases} A_j \sin(k_j^L x) & 0 \le x \le x_c, \\ A_j \beta_j \sin[k_j^R (x - L)] & x_c \le x \le L, \end{cases} \tag{4.7}$$

where $\beta_j = \frac{\sin(k_j^L x_c)}{\sin[k_j^R (x_c - L)]}$, and we have wavevectors $k_j^2 = \omega_j^2 \ell(x) c$. The constant A_j simply scales $X_j(x)$ to ensure orthogonality $\int_0^L \ell(x) X_m X_n \, dx = \delta_{mn}$ of the modes.

To find the $\{\omega_j\}$, Eq. (4.5) is integrated over the infinitesimally small region $x_c \pm \delta$ yielding

$$\beta_j k_j^R \cos\left(k_j^R \left[x_c - L\right]\right) - k_j^L \cos\left(k_j^L x_c\right) - \frac{c}{C_c} \sin\left(k_j^L x_c\right) = 0. \tag{4.8}$$

This is a key equation, all effects of the capacitor and altered inductance are essentially encapsulated in these modified wavevectors.

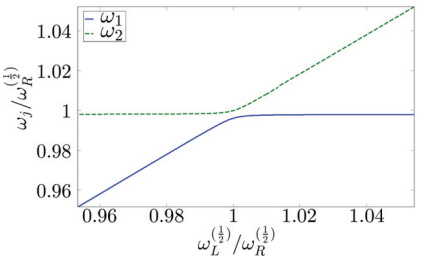

Figure 4.2. Frequencies of the lowest two modes, with $x_c = L/2$, as a function of $\omega_L^{(\frac{1}{2})} = 2\pi/(L\sqrt{\ell_L c})$.

If we examine the case $x_c = L/2$, then taking the limit $C_c \to 0$ would result in two isolated cavities of equal length. These left and right half-cavities, have the fundamental frequencies $\omega_{L(R)}^{(\frac{1}{2})} = 2\pi/(L\sqrt{\ell_{L(R)} c})$. Figure 4.2 shows the two lowest eigenfrequencies ω_1 and ω_2, calculated numerically from Eq. (4.8), as a function of $\omega_L^{(\frac{1}{2})}$. If $\ell_L = \ell_R$, the isolated left and right cavities are in resonance, i.e., $\omega_L^{(\frac{1}{2})} = \omega_R^{(\frac{1}{2})}$; in reality the finite capacitance couples the two cavities, and results in an avoided crossing for the two lowest energy modes of the total system. Away from this resonance point, the lowest angular frequency ω_1, is approximately equal to $\omega_L^{(\frac{1}{2})}$, when $\ell_L \gg \ell_R$. In this case, we find for the second mode, $\omega_2 \approx \omega_R^{(\frac{1}{2})}$ (and vice-versa for $\ell_L \ll \ell_R$). With a tunable inductance, we may therefore switch the lowest-energy excitations of the coupled cavity system between the left and right cavities.

To illustrate this point further, let us consider the mode profiles. In Fig. 4.3(a), we take $x_c = L/2$ with $\ell_L \neq \ell_R$. In this setup, we observe that by tuning ℓ_L, we can move from a cavity whose first excited photon

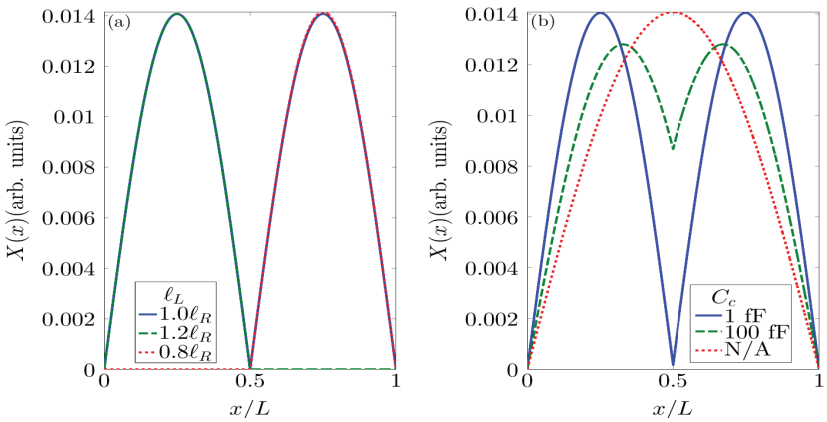

Figure 4.3. Mode profiles as a function of the position in the cavity. In (a), the capacitor is positioned at $x_c = L/2$ with a capacitance $C_c = 1$ fF, while the inductance per unit length in the left of the cavity is varied between $\ell = 0.8\ell_R$ (dotted line), $\ell = \ell_R$ (solid line), and $\ell = 1.2\ell_R$ (dashed line). In (b), $x_c = L/2$, the inductance is constant, $\ell_L = \ell_R$, and we take no capacitor (dotted line), $C_c = 100$ fF (dashed line), and $C_c = 1$ fF (solid line).

state is predominantly found in the left hand side of the cavity, to one in which it is predominantly in the right hand side, via a region where it is a mixture of both left and right. In Fig. 4.3(b), we again take $x_c = L/2$ but fix $\ell_L = \ell_R$. The first current mode for several values of C_c is then shown, and we observe that for small C_c the current is virtually zero at the position of the capacitor, and hence the single cavity has essentially been divided into two.

As demonstrated in Publication III, we may continue to quantize the charge operator $\hat{\Theta}$ as

$$\hat{\Theta}_j(x,t) = \begin{cases} \sqrt{\frac{\hbar A_j^2}{2\omega_j}}\left[\hat{a}_j + \hat{a}_j^\dagger\right]\sin(k_j^L x), & 0 \le x \le x_c, \\ \beta_j\sqrt{\frac{\hbar A_j^2}{2\omega_j}}\left[\hat{a}_j + \hat{a}_j^\dagger\right]\sin[k_j^R(x-L)], & x_c \le x \le L, \end{cases} \tag{4.9}$$

which results in the current $\hat{I} = \frac{\partial\hat{\Theta}}{\partial t}$, and voltage $\hat{V} = \frac{1}{c}\frac{\partial\hat{\Theta}}{\partial x}$, operators

$$\hat{I}_j(x,t) = \begin{cases} i\sqrt{\frac{\hbar A_j^2}{2\omega_j}}\omega_j\left[\hat{a}_j^\dagger - \hat{a}_j\right]\sin(k_j^L x), & 0 \le x \le x_c, \\ i\beta_j\sqrt{\frac{\hbar A_j^2}{2\omega_j}}\omega_j\left[\hat{a}_j^\dagger - \hat{a}_j\right]\sin[k_j^R(x-L)], & x_c \le x \le L, \end{cases} \tag{4.10}$$

and

$$\hat{V}_j(x,t) = \begin{cases} \frac{k_j^L}{c}\sqrt{\frac{\hbar A_j^2}{2\omega_j}}\left[\hat{a}_j + \hat{a}_j^\dagger\right]\cos(k_j^L x), & 0 \le x \le x_c, \\ \frac{k_j^R\beta_j}{c}\sqrt{\frac{\hbar A_j^2}{2\omega_j}}\left[\hat{a}_j + \hat{a}_j^\dagger\right]\cos[k_j^R(x-L)], & x_c \le x \le L, \end{cases} \tag{4.11}$$

where we have employed the Heisenberg picture with $\partial_t\hat{a}_j = -i\omega_j\hat{a}_j$, and $\partial_t\hat{a}_j^\dagger = i\omega_j\hat{a}_j^\dagger$. These current and voltage operators should be compared with Eqs. (4.1) and (4.2).

4.2 Classical Matrix Analysis

The quantum model provides an analytic solution for the current and voltage operators for a given ω_j, however it is not trivial to include dissipation in such a formalism. We therefore also consider a classical analysis of this circuit model, previous classical studies having proved useful in analysing the low-temperature photonic heat conduction via a transmission line [70].

Let us first consider a resonator which has been modified only by inserting a capacitance C_c at node k. Once again, our starting point is the distributed-element model of the transmission line shown in Fig. 4.1, where the current flowing into node n is denoted by I_n. Application of Kirchoff's Laws gives

$$(-LC\omega_j^2 + 2)I_n - I_{n-1} - I_{n+1} = 0, \quad n \neq k, \tag{4.12}$$

$$\left(-LC\omega_j^2 + 2 + \frac{C}{C_c}\right) I_k - I_{k+1} - I_{k-1} = 0. \tag{4.13}$$

We assume that there is a common eigenmode across the two cavities, which may be written in the form $I_j(x,t) = I(x)e^{i\omega_j t}$. Equations (4.12) and (4.13) are then equivalent to the eigenproblem $MI(x) = \omega_j^2 I(x)$, with a tridiagonal matrix M

$$M = \frac{1}{LC}\begin{pmatrix} \ddots & \ddots & \ddots & & & & \\ & -1 & 2 & -1 & & & \\ & & -1 & 2+\frac{C}{C_c} & -1 & & \\ & & & -1 & 2 & -1 & \\ & & & & \ddots & \ddots & \ddots \end{pmatrix}, \tag{4.14}$$

which has a Laplacian form, with the diagonal element in the kth row, modified to be $M(k,k) = \frac{1}{LC}\left(2 + \frac{C}{C_c}\right)$. The eigenvectors and eigenvalues of M give the spatial mode profile and the angular frequencies respectively.

It is relatively easy to incorporate SQUIDs into this matrix, the typical width of a SQUID is approximately $10\,\mu$m, much less than the length of the microwave transmission lines considered here, and hence we can assume that the SQUIDs change the impedance only at a single node[2]. We therefore replace L with $L + L_J$ [see Eq. (2.1)] at the relevant nodes in Fig. 4.1, which translate into a scaling of the corresponding rows of M by

[2]For a very dense discretisation, each SQUID may affect several nodes, in this case the SQUID inductance is just divided between them in a linear manner.

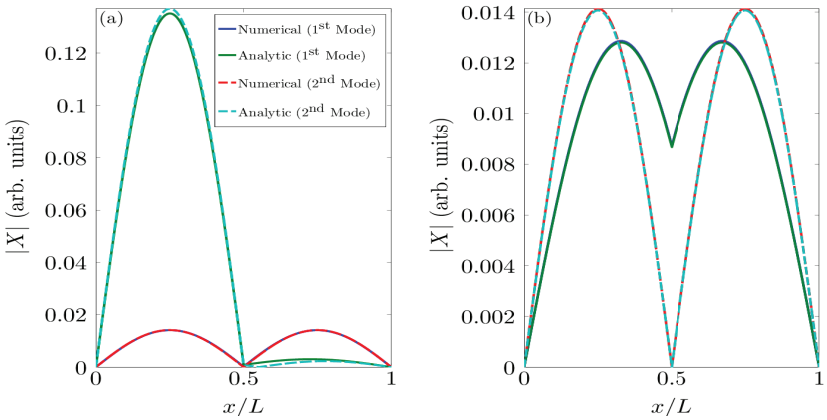

Figure 4.4. Comparison of the first mode (solid lines) and second mode (dashed line) computed using the analytical result of Eq. (4.7), and by diagonalising the matrix of Eq. (4.14). In both (a) and (b), we take a capacitor positioned at $x_c = L/2$ with $C_c = 1$ fF. In (a) we have $\ell_L = 1.2\ell_R$, whereas in (b), $\ell_L = \ell_R$.

a factor of $L/(L + L_s)$. In Fig. 4.4, we compare the first and second modes calculated using this method to those given by the analytic solution of Sec. 4.1, and observe good agreement. If further accuracy is required the small remaining discrepancy can be removed by increasing the number of points used in the discretisation.

We now include a resistor of size $R = r\Delta x$ at the rth node of the lumped element model. The preceding analysis is unaffected except at $n = r$, at which point the voltage across the resistor fluctuates due to the thermal noise. We therefore associate a noise voltage $\delta V(t)$ with node r and apply Kirchoff's Laws to find

$$\left(-LC\partial_t^2 - CR\partial_t - 2\right) I_r + I_{r-1} + I_{r+1} = C\delta\dot{V}_r(t). \tag{4.15}$$

To see the effect on the mode profile, we first assume that the resistor does not introduce any noise, in which case we may set $\delta V(t) = 0$. In this case, Eq. (4.15) along with Eqs. (4.12) and (4.13) no longer form an eigensystem but instead take the form $Z(\omega)I(x) = 0$, where $Z(\omega)$ is an 'impedance' matrix, similar in form to Eq. (4.14). For a non-trivial solution of $I(x)$, we have the condition that

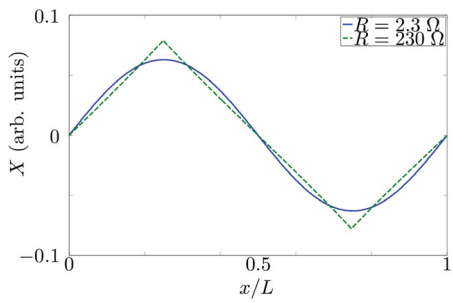

Figure 4.5. Profiles of the fundamental current mode, when a resistor of resistance 2.3Ω (solid line) and 230Ω (dashed line) is inserted into the line. The latter does not propagate.

$\det[Z(\omega)] = 0$, enabling us to calculate the eigenfrequency, ω_j. The elements of $I(x)$ can then be found in a systematic manner from $Z(\omega_j)$. To handle $\delta V(t)$, as we must do, for example, to calculate the classical power transfer we can move to Fourier space, as discussed in Publication II.

Figure (4.5) shows that adding a resistor into the line can distort the mode profile substantially. The coupling to the mode of a $230\ \Omega$ resistor positioned at $L/4$ is so great that the imaginary part of the eigenfrequency becomes orders of magnitude greater than the real part and these modes therefore do not propagate. In contrast, placing a resistor with $R = 2.3\ \Omega$ at the same location results in an almost negligible change of the profile and frequency. A more quantitative criterion for the maximum acceptable resistor coupling is given in Chapter 5.

A key message of this thesis is that changes to the sinusoidal mode profile of the bare resonator can play a significant role in designing and understanding experiments. Much of our work will involve inserting additional components into the line, some of which can have a dramatic effect on the mode profiles. Quantifying these effects forms a major part of Publication II, and is crucial in the analysis of Publication III.

5. Single-Photon Heat Transfer in a Cavity

This chapter covers single-photon heat conduction in a cavity, the subject of Publications I and II. Inspired by the experiments described in Chapter 3, which demonstrated the first observations of quantum-limited photonic heat conduction, we propose a related circuit consisting of a coplanar waveguide cavity. In a cavity, the excitations are photons of well defined frequencies, and we are therefore able to identify individual photons as the source of the heat conduction between the resistors. Experimental verification of these results would be an important first step on the road to developing useful normal-metal components for cQED.

5.1 Calculation of the Photonic Heat Power in a Cavity

An illustration of the cavity discussed here is shown in Fig. 5.1. It has been modified by the introduction of two resistors into the central conduction line. These are placed close to the ends of the line such that they couple only weakly to the modes of the cavity. In this case, the contribution of the cavity to the Hamiltonian takes the usual form $\hat{H}_{\text{cav}}(t) = \sum_j \hbar\omega_j(\hat{a}_j^\dagger\hat{a}_j + 1/2)$, i.e., a sum of harmonic oscillators with photon number eigenstates $|n\rangle_j$, at the frequencies of the standard cavity $\omega_j = j\pi/(L\sqrt{\ell c})$. The Hamiltonian of the ith resistor $\hat{H}_R^{(i)}$, can also be represented as an infinite number of harmonic oscillator modes [77], though when calculating the transition rates we will trace out these degrees of freedom, and so the explicit form of $\hat{H}_R$ plays no role in the analysis presented here. Finally, the total Hamiltonian will contain a term $\hat{H}_{\text{int}}$, corresponding to the interaction between the resistors and the cavity modes. The total Hamiltonian is therefore expressed as $\hat{H}(t) = \hat{H}_{\text{cav}}(t) + \hat{H}_R^{(1)} + \hat{H}_{\text{int}}^{(1)}(t) + \hat{H}_R^{(2)} + \hat{H}_{\text{int}}^{(2)}(t)$.

We treat the resistors as the dominant environment for the cavity, stimulating photonic emission and absorption through $\hat{H}_{\text{int}}$. We then proceed

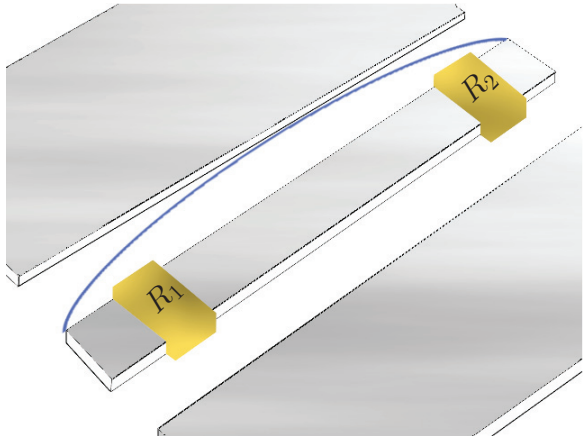

Figure 5.1. Coplanar waveguide cavity with two resistors embedded into the central conduction line. The blue line represents the magnitude of the current in the first mode.

to calculate the rates for resistor induced transitions, and the resulting photonic heat power into each resistor.

In the weak coupling regime, it can be shown that applying Fermi's golden rule to an interaction term of the form $\hat{H}_{\rm int}(t) = \sum_j \hat{Q}_j \otimes \delta\hat{E}(t)$, in which $\hat{Q}_j$ acts only on the system degrees of freedom, and $\delta\hat{E}$ only on those of the environment, yields the transition rates [68]

$$\Gamma^j_{m\to l} \approx \frac{|\langle l|\hat{Q}_j|m\rangle|^2}{\hbar^2} S_E(-\omega_{ml}), \tag{5.1}$$

between states $|m\rangle$ and $|l\rangle$ of the jth mode. Here $\omega_{ml} = \frac{E^j_l - E^j_m}{\hbar}$ corresponds to the energy change in the transition, and $S_E(\omega)$ is the spectral density of the environmental fluctuations causing the transition.

In our case, we treat the resistor as a semi-classical voltage source with fluctuations governed by the thermal Johnson-Nyquist noise [Eq. (3.1)]. If these fluctuations are small, the cavity-resistor interaction Hamiltonian can be written as $\hat{H}_{\rm int} = \hat{\Theta}_L(x_R) \otimes \delta\hat{V}$, as shown in Publication I. We thus apply Eq. (5.1) to find the rates for resistor i to increase or decrease the photon number in the jth mode to be

$$\Gamma^{(i),j}_{n\to n+1} = (n+1)\frac{2R_i \sin^2(k_j x^i_r/L)}{L\ell} \frac{1}{\exp\left(\frac{\hbar\omega_j}{k_B T_i}\right) - 1}, \tag{5.2}$$

$$\Gamma^{(i),j}_{n\to n-1} = n\frac{2R_i \sin^2(k_j x^i_r/L)}{L\ell} \frac{1}{1 - \exp\left(\frac{-\hbar\omega_j}{k_B T_i}\right)}, \tag{5.3}$$

for weak resistor-cavity coupling. The voltage fluctuations of the two resistors are not intrinsically correlated and therefore the total rate is just the sum of the two individual contributions $\Gamma^j_{n\to n+1} = \Gamma^{(1),j}_{n\to n+1} + \Gamma^{(2),j}_{n\to n+1}$.

Naturally, inserting resistors into the cavity will substantially increase the dissipation. We require that the Q-factor remains $\gtrsim 10$, so that each photon is still able to make a reasonable number of oscillations before it decays. For an n-photon state, the excitation probability decays as[1] $p_n(t) = e^{-2t\Gamma^{(1),j}_{n\to n-1}}$. Denoting E as the energy stored in the cavity, and $\Delta E = E(t=0) - E(t=1/f_j)$ the energy lost after one oscillation, Q_n is by definition

$$Q_n = \frac{2\pi E}{\Delta E} = 2\pi \frac{n\hbar\omega}{\hbar\omega\left[1-\exp\left(-\frac{2n\Gamma^{(1),j}_{1\to 0}}{f_j}\right)\right]} \approx \frac{\pi f_j}{\Gamma^{(1),j}_{1\to 0}}, \tag{5.4}$$

for each number state $|n\rangle_j$. Taking the zero temperature rates, we arrive at a limit to the coupling strength for symmetric resistance

$$Q_n \approx \frac{j\pi}{4}\frac{Z_c}{R^{(j)}_{\text{eff}}} \gg 1, \tag{5.5}$$

where we have defined an effective resistance $R^{(j)}_{\text{eff}} = R_1 \sin^2(j\pi x^1_r/L)$ and the characteristic impedance of the cavity $Z_c = \sqrt{\frac{\ell}{c}}$.

We denote the eigenstate occupation probability for each mode by the vector $\vec{p}^{\,j}$, each element of which, p^j_n, represents the probability to be in the corresponding photon number state $|n\rangle_j$. The master equation describing the time evolution of $\vec{p}^{\,j}$, may then be expressed as a first-order differential equation $\frac{d\vec{p}^{\,j}(t)}{dt} = \Gamma^j \vec{p}^{\,j}(t)$, for each mode j. We have employed the secular approximation, so that the evolution of the probabilities of the eigenstates decouples from their coherence, justifying this treatment. The probability distribution in steady state therefore corresponds to the zero eigenvalue of the transition matrix Γ^j.

Figure 5.2(a) shows the setup schematically, with both resistors continuously emitting and absorbing photons to and from a shared cavity. For each photon number state, the rate at which energy is absorbed by resistor i is equal to the probability p^j_n, of having n photons in the mode, multiplied by the energy difference $\hbar\omega_j$, of the transition, and by the net photon number absorption rate for the transition. To obtain the total power, we sum over all modes and photon numbers

$$P^{(i)}_{\text{net}} = \sum_j \hbar\omega_j \sum_n \left(\Gamma^{(i),j}_{n\to n-1} - \Gamma^{(i),j}_{n\to n+1}\right) p^j_n. \tag{5.6}$$

Why do we refer to single-photon heat conduction? At temperatures $k_B T \ll \hbar\omega_1$, the probability to simultaneously excite multiple photons or higher

[1] For the sake of this argument we assume the resistors have the same resistances, relative offsets, and temperatures, hence we get a factor of two in the exponent.

modes is suppressed exponentially with decreasing temperature. The overwhelming majority of the heat conduction therefore takes place at the single-photon level. Figure 5.2(b), presents a comparison of the full solution [Eq. (5.6)], with the two-level approximation which confirms that the lowest energy state of the cavity accounts for the vast majority of the heat power at temperatures below 90 mK.

In the two-level approximation, there may be only zero or one photons in the fundamental mode and, in steady state, the net photon power transferred into the ith resistor may be calculated analytically (see Publication I) as

$$P_{\text{net}}^{(i)} = \Gamma_{1\to0}^{(i),1} p_1 \hbar\omega_1 - \Gamma_{0\to1}^{(i),1} p_0 \hbar\omega_1 = \frac{\hbar\omega_1}{\Gamma^{\Sigma}} \left(\Gamma_{1\to0}^{(i),1} \Gamma^{+} - \Gamma_{0\to1}^{(i),1} \Gamma^{-} \right), \qquad (5.7)$$

here we have defined the rate to add $\Gamma^{+} = \Gamma_{0\to1}^{(1),1} + \Gamma_{0\to1}^{(2),1}$, and to remove $\Gamma^{-} = \Gamma_{1\to0}^{(1),1} + \Gamma_{1\to0}^{(2),1}$, a photon, as well as a total rate $\Gamma^{\Sigma} = \Gamma^{-} + \Gamma^{+}$.

5.2 Remote Heating and Cooling of a Dissipative Cavity Element

The final part of this chapter is devoted to the calculation of remote heating and refrigeration of one of the metal islands in the cavity. To achieve this, NIS probes are employed in order to vary T_1, the temperature of the first resistor. We then calculate the temperature of the second island, T_2 when the system has reached steady state. At this quasiequilibrium point, the net heat power from all sources into each of the resistors must balance. We include only the power resulting from the interaction between the electrons in the resistor with the phonons in the substrate, and the net photon power transferred as a result of exchange between the resistors and the cavity P_{Γ} [Eq. (5.6)]. The phonon power [66], $P_{\Sigma}^{(i)} = \Sigma V (T_i^5 - T_0^5)$, is dependent on the material-specific constant Σ, the volume of the resistors V, and the temperature of the phonons, which we assume to be at the bath temperature T_0. In this simple case, we find the steady state temperature of the second resistor to be[2]

$$T_2 = \sqrt[5]{P_{\Gamma}/(\Sigma V) + T_0^5}. \qquad (5.8)$$

Since P_{Γ} is itself a function of T_2, Eqs. (5.8) and (5.6) must be solved self-consistently. We may also define the effective temperature of the cavity

[2]Inevitably there are several additional sources of power other than those discussed here, e.g., from the NIS probes or due to quasiparticle excitations. These are accounted for in Publication II, where it is demonstrated that they do not essentially alter the results, I therefore do not discuss them further.

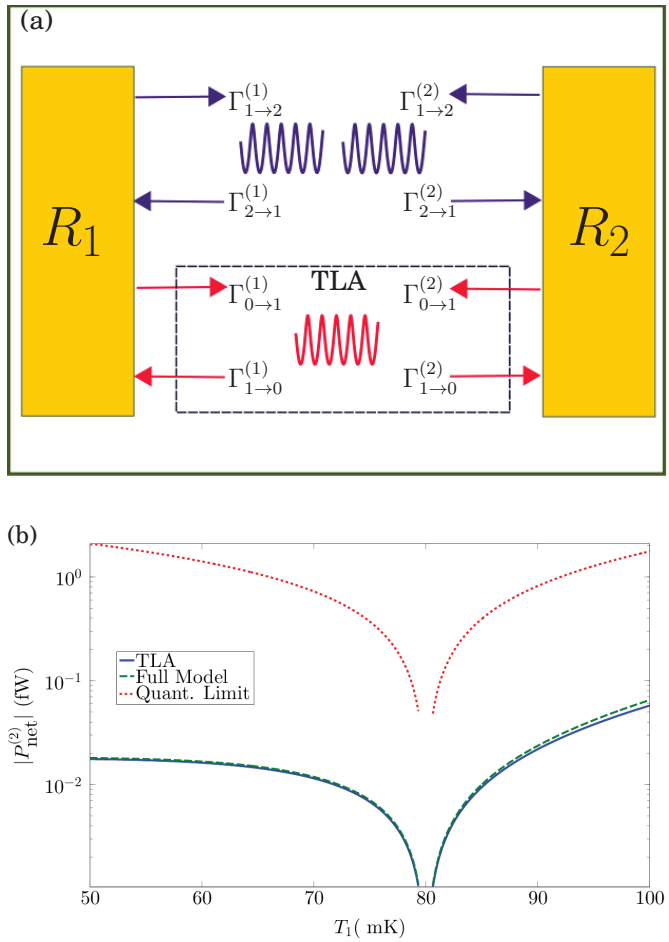

Figure 5.2. (a) Schematic diagram showing the resistor-induced transitions between the two lowest energy states of the first cavity mode. The two-level approximation (TLA) is marked with the dashed box. (b) Comparison of the photonic power into the second resistor using multiple modes and excitations (solid line), with the TLA (dashed line), and the quantum-limited power (dotted line), as a function of the temperature of resistor 1. The latter is calculated as $P^{(i)}_{\rm net} = g_0(T_{\rm eff})\Delta T$, where the effective cavity temperature $T_{\rm eff}$, is calculated according to Eq. (5.9), and $\Delta T = T_1 - T_2$. The temperature of the first resistor is scanned from 50 to 100 mK while the second resistor is held at a fixed temperature of 80 mK. The length of the cavity is $L = 6.4$ mm, it has a capacitance per unit length $c = 130$ pF, and a characteristic impedance $Z_c = 50\ \Omega$. This results in cavity modes with angular frequencies $\omega_j = 2j\pi \times 12.0$ GHz $= 577$ mK $\times \frac{jk_B}{\hbar}$. The resistors are offset from the ends of the cavity by $L/30$ with resistances $R = 230\ \Omega$, yielding $R_{\rm eff} = 2.5\ \Omega$, for the lowest mode.

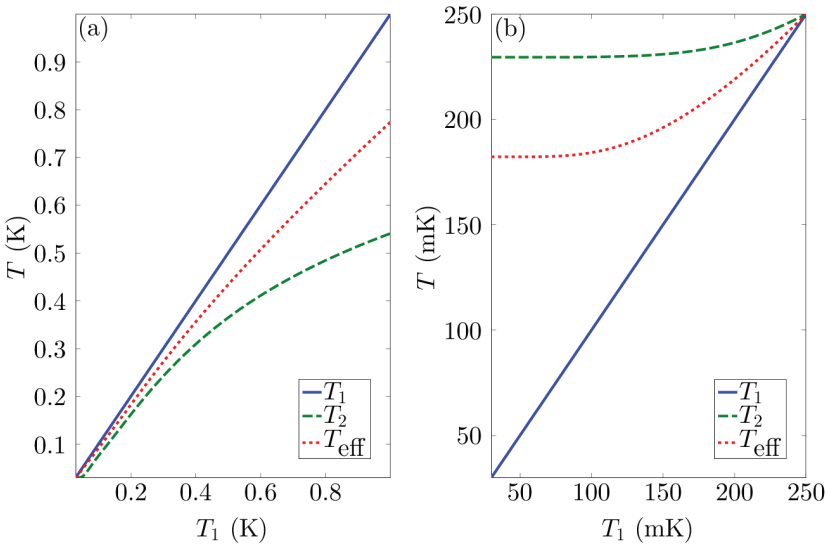

Figure 5.3. Temperature of resistor 2 (dashed line) and the effective temperature of the cavity (dotted line) as functions of the temperature of resistor 1, which is also shown for comparison (solid line). In (a) we observe heating of resistor 2 above the phonon bath temperature $T_0 = 30$ mK, and in (b) cooling below the bath temperature of 250 mK. The cavity has a capacitance per unit length, $c = 130$ pF and a characteristic impedance $Z_c = 50\,\Omega$. The length of the cavity is $L = 6.4$ mm, with resistors offset from the ends by $L/30$ with resistance $R = 230\,\Omega$. The angular frequency of the lowest cavity mode is $\omega_1 = 577$ mK $\times \frac{k_B}{\hbar}$.

as [68]

$$T_{\text{eff}} = \frac{\hbar\omega_{01}}{k_B \log\left(\frac{\Gamma_{1\to 0}}{\Gamma_{0\to 1}}\right)}. \tag{5.9}$$

We show the resulting T_2 in Fig. 5.3. In Fig. 5.3(a), T_1 is scanned over the range between 30 mK and 1 K, with a phonon bath temperature of 30 mK. We observe that the photonic power is dominant if T_1 is below 200 mK. In this region, T_2 follows T_1 very closely, allowing us to control the temperature of resistor 2 at will. At $T_1 > 200$ mK, the phonon contribution becomes notably more significant, and the effect of the heating on T_2 becomes weaker. In Fig. 5.3(b), we increase the bath temperature to 250 mK and then vary T_1 from 250 mK to 40 mK. We observe that the second resistor is cooled, with T_2 saturating about 20 mK below T_0. By modifying the effective resistance [within the constraints of Eq. (5.5)] we are able to vary the coupling strength and alter this saturation temperature. For the parameters employed in Fig. 5.3, we have from Eq. (5.5), $Q \approx 20$ for the cavity quality factor.

Experimental observation of this heating and cooling would be not only a demonstration of single-photon heat conduction, but also show that the resistors act as as an engineered artificial environment for the cavity.

6. Tunable Environment for Superconducting Qubits

In this chapter, we utilise the framework that we have developed to integrate normal-metal islands into superconducting cavities, and consider an application for quantum computing. Covering the works of Publications III and IV, our aim is to demonstrate that the coupling of a qubit to its artificial environment can be tuned *in situ*. Here, one can quickly switch between a setup in which the resistor is the dominant environment for the qubit, causing rapid qubit initialisation, to one in which the coupling is so weak that it is no longer the limiting factor for qubit decoherence. We begin with the distributed-element model which includes the full spatial dependence of the modes. Subsequently, we consider a more accessible model in which two coupled resonators are modelled as LC circuits.

6.1 Distributed-Element Cavity Model

We propose the setup shown schematically in Fig. 6.1. A capacitor is used to divide a single cavity into two weakly coupled cavities, designated as left and right. We introduce a resistor into the left cavity, along with a set of SQUIDs, which permit the inductance per unit length of this cavity to be tuned. Into the right cavity, we place only a qubit and hence it retains a very high internal quality factor. We analyse this scheme using the circuit representation of Fig. 4.1. The cavity frequency is calculated using Eq. (4.8), which incorporates the effects of the coupling capacitor and variable cavity inductance. Any small effects of the resistor and qubit on the profile are neglected. The qubit will, however, couple to the cavity and affect the eigenstates. Modelling the qubit as a dipole moment, $\hat{d} = d\hat{\sigma_x}$, and employing the rotating wave approximation [78], gives a dipole–

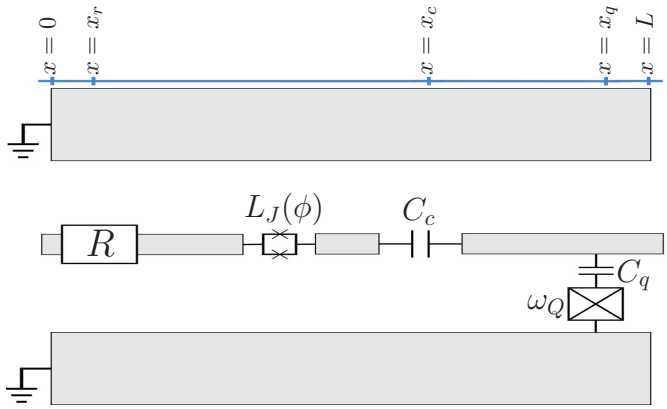

Figure 6.1. Schematic illustration of a qubit (rightmost structure) coupled to a superconducting cavity with an artificial environment R. Adapted from Publication III.

electric-field interaction of the form

$$\hat{H}^q_{\text{int}} = -\sum_j \hat{d} \cdot \hat{E}_j(x_q) = \sum_j \hbar g_j (\hat{\sigma}^+ \hat{a} + \hat{\sigma}^- \hat{a}^\dagger). \tag{6.1}$$

For concreteness, we consider a charge qubit with Josephson energy E_J, charging energy E_C, and junction capacitance C_J. For such a qubit, a more thorough treatment in the transmon regime [36, 79] yields a coupling strength

$$g_j = -\sqrt{2}\left(\frac{E_J}{8E_C}\right)^{1/4} \frac{C_q}{C_\Sigma} \frac{e}{\hbar} \frac{k_j^R \beta_j \vartheta_j}{c} \cos[k_j^R (x_q - L)], \tag{6.2}$$

where the qubit couples to the center conductor with capacitance C_q at position x_q. The total capacitance C_Σ is defined as $C_J + C_q$. The wavevector, k_j^R, angular frequency, ω_j, asymmetry factor, β_j, and normalisation constant, A_j, of the mode were all introduced in Chapter 4. The capacitance per unit length of the center conductor has a value of c.

With a single cavity mode, we may identify the Hamiltonian $\hat{H}^q_{\text{int}}$ (see Publication III) as the Jaynes-Cummings Hamiltonian with the excited eigenstates [36]

$$|-, n\rangle = \cos(\theta_n)|g, n\rangle - \sin(\theta_n)|e, n-1\rangle \tag{6.3}$$

$$|+, n\rangle = \sin(\theta_n)|g, n\rangle + \cos(\theta_n)|e, n-1\rangle \tag{6.4}$$

and energies

$$E_{\pm,n} = \frac{\hbar}{2}\left[(n-1)\omega_r + \omega_a \pm \sqrt{4ng^2 + \Delta^2}\right], \qquad n \neq 0, \tag{6.5}$$

where $\Delta = \omega_Q - \omega_1$, is the detuning of the qubit and cavity frequencies, and $\theta_n = \arctan(2g\sqrt{n}/\Delta)/2$. In this single-mode case, we can find analytic

expressions for the rates. The first two excited states decay to the ground state at a rate

$$\Gamma_{1\to 0} = A_1^2 \frac{E_1}{\hbar\omega_1} \frac{\sqrt{4g^2+\Delta^2}+\Delta}{2\sqrt{4g^2+\Delta^2}} \frac{R\sin^2(k_1^L x_r)}{1-\exp[-E_1/(k_B T)]}, \tag{6.6}$$

$$\Gamma_{2\to 0} = A_1^2 \frac{E_2}{\hbar\omega_1} \frac{\sqrt{4g^2+\Delta^2}-\Delta}{2\sqrt{4g^2+\Delta^2}} \frac{R\sin^2(k_1^L x_r)}{1-\exp[-E_2/(k_B T)]}, \tag{6.7}$$

where the normalisation constants A_j, introduced in Chapter 4, can depend strongly on the cavity parameters

$$A_j = \left\{ \frac{\ell_L}{4k_j^L}\left[2k_j^L x_c - \sin(2k_j^L x_c)\right] - \frac{\ell_R \beta^2}{4k_j^R}\left[2k_j^R(x_c - L) - \sin(2k_j^R(x_c - L)\right] \right\}^{-1/2}. \tag{6.8}$$

The reverse transitions are of identical form and can be found by making the substitution $E_i \to -E_i$. If the detuning is large ($\Delta/g \gg 1$), then the Jaynes-Cummings eigenstates are approximately equivalent to the basis states $|\sigma, n\rangle$, that is $|-,1\rangle \approx |g,1\rangle$, and $|+,1\rangle \approx |e,0\rangle$.

More generally, we consider an extended Jaynes-Cummings Hamiltonian with two cavity modes. We diagonalise this Hamiltonian to find the eigenvectors and energies numerically and then construct the transition rates as above. Though we no longer arrive at a closed form expression for the rates, the procedure is conceptually identical to the single-mode case (see Publication III).

Once we have the transition rates, the evolution of the probability is determined by the master equation

$$\frac{d\vec{p}(t)}{dt} = \Gamma\vec{p}(t) \Rightarrow \vec{p}(t) = \exp\left[\Gamma t\right]\vec{p}(0), \tag{6.9}$$

allowing us to simulate the dynamics. In Fig. 6.2 we show the decay of the eigenstates corresponding to excitations of the qubit and the lowest energy photon mode in the single-mode limit, which we focus on for simplicity. Three distinct features are observed. Firstly, if the left and right half-cavities are in resonance, the amplitude of the lowest-energy mode is significant in both cavities, such that qubit is strongly coupled to this mode, which is itself strongly coupled to the resistor. Quick decay of both photon and qubit are observed here. Secondly, if the left half-cavity is then tuned above resonance, the qubit remains strongly coupled to the lowest-energy mode. However, the mode couples here only weakly to the resistor, as a result of its very small amplitude in the left cavity. This results in slow decay of both photon and qubit. In the third case, the left half-cavity

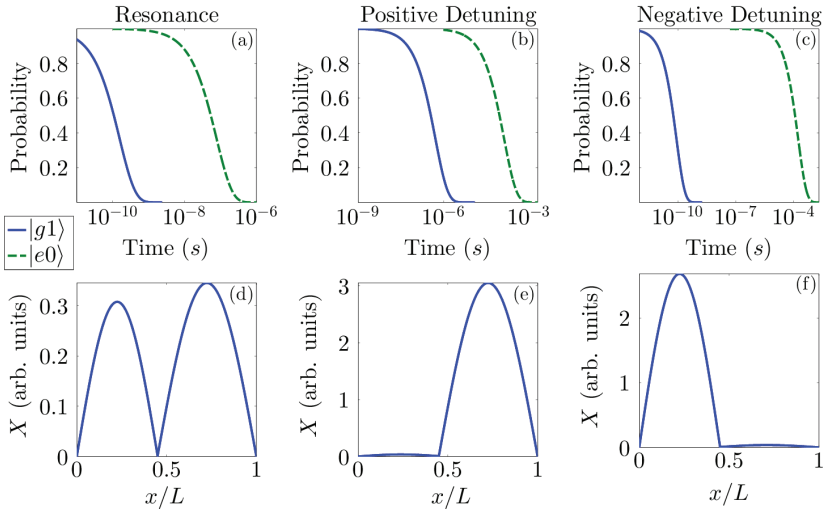

Figure 6.2. (a), (b), and (c): Probability of the system to be in the eigenstate corresponding to $|g1\rangle$ (solid line) and $|e0\rangle$ (dashed line), as a function of time when the system is initially prepared in these eigenstates. (d), (e), and (f): Current profile of the lowest-energy mode corresponding to $|g1\rangle$ [Eq (4.7)], for (a), (b), and (c), respectively. We focus on three cases, distinguished by the relative magnitudes of the isolated left and right cavity frequencies, $\omega_L^B = \pi/(x_c\sqrt{\ell_L c})$, and $\omega_R^B = \pi/[(L-x_c)\sqrt{\ell_R c}]$. In resonance $\omega_L^B \approx \omega_R^B$, and the two frequencies differ only by $\omega^{\rm res} = 2\pi \times 15$ MHZ, which corresponds to the cavity interaction energy. From this resonance point, ω_L^B is tuned by $\pm 42\omega^{\rm res}$, for positive and negative detuning, respectively. By varying the inductance of the left hand side, we can tune ω_L^B, and switch between these three cases. For the cavity parameters, we take a cavity length $L = 12$ mm, with a capacitance per unit length for the central conducting strip, $c = 130 \times 10^{-12}$ Fm^{-1}. The characteristic impedance of the right cavity is $Z_c = \sqrt{\ell_R/c} = 50\ \Omega$. A capacitance $C_c = 1$ fF, is positioned at $x_c = 0.45L$, in addition to a resistance of $R = 230\ \Omega$, positioned with an offset $x_r = L/25$. The angular frequencies for left-right cavity resonance [(a),(d)], are $\omega_1 = 2\pi \times 11.64$ GHz, for positive detuning [(b),(e)], $\omega_1 = 2\pi \times 11.65$ GHz, and for negative detuning [(c),(f)], $\omega_1 = 2\pi \times 11.02$ GHz. The qubit detuning to the first mode Δ, is held constant at $2\pi \times 979$ MHz. These calculations are performed using the single-mode model; in the general case, at least two modes should be considered (see Publication III) .

is tuned below resonance. In this configuration, the qubit is only weakly coupled to the lowest-energy mode, and the mode is strongly coupled to the resistor. Thus the photon decays rapidly but the qubit remains protected. By tuning the flux through the SQUIDs we can move continuously between these three cases (see Sec. 4.1). As shown in Publication III, if we also vary the qubit-cavity detuning Δ, we can access an even wider range of decay times. In the two-mode case, the noise source for each mode is not independent, and consequently we cannot simply infer the qualitative behaviour directly from Fig. 6.2. Nevertheless, as described in detail in Publication III, by also utilising the left-cavity–qubit resonance, variation of the qubit lifetime over many orders of magnitude still remains attainable.

6.2 Lumped-Element Resonator System

In this section, we study a closely related, but more convenient system, of two coupled lumped element oscillators which are themselves capacitively coupled to a qubit and a resistor in the circuit configuration shown in Fig. 6.3(a). In comparison to the galvanic connection employed in Sec. 6.1, this capacitive bath coupling can potentially simplify the fabrication of the devices. This section concludes with the introduction of a mapping between the resonator parameters and those of the distributed-element system, such that this lumped-element model can also be utilised to simulate the dynamics of the coupled cavity system.

The complete Hamiltonian of this setup may be written as

$$\begin{aligned}\hat{H}_{\text{tot}} = &\overbrace{\frac{1}{2}\tilde{C}_L\hat{\tilde{V}}_L^2 + \frac{1}{2}L_L\hat{\tilde{I}}_L^2}^{\hat{\tilde{H}}_L} + \overbrace{\frac{1}{2}\tilde{C}_R\hat{\tilde{V}}_R^2 + \frac{1}{2}L_R\hat{\tilde{I}}_R^2}^{\hat{\tilde{H}}_R} + \overbrace{\frac{1}{2}C_c(\hat{\tilde{V}}_L - \hat{\tilde{V}}_R)^2}^{\hat{H}_{C_c}} + \\ &\overbrace{\frac{1}{2}C_E(\hat{\tilde{V}}_L - \delta\hat{V}_r)^2}^{\hat{H}_{C_E}} + \overbrace{E_J\cos(\hat{\phi}) + \frac{1}{2}C_J\hat{V}_q^2}^{\hat{\tilde{H}}_q} + \overbrace{\frac{1}{2}C_q(\hat{\tilde{V}}_R - \hat{V}_q)^2}^{\hat{H}_{C_q}} + \\ &\overbrace{\sum_r \hbar\omega_r\left(\hat{a}_r^\dagger\hat{a}_r + \frac{1}{2}\right)}^{\hat{\tilde{H}}_r},\end{aligned} \tag{6.10}$$

where $\hat{\tilde{H}}_{L(R)}$ is the Hamiltonian of the left (right) resonator, which consists of an inductor $L_{L(R)}$, and capacitor $\tilde{C}_{L(R)}$. We denote by $\hat{\tilde{V}}_{L(R)}$, the voltage across the respective capacitors, and by $\hat{\tilde{I}}_{L(R)}$, the current through the respective inductors. The voltage across the resistor is $\delta\hat{V}_r$. The energy of the resonator coupling, resistor coupling, and qubit coupling capac-

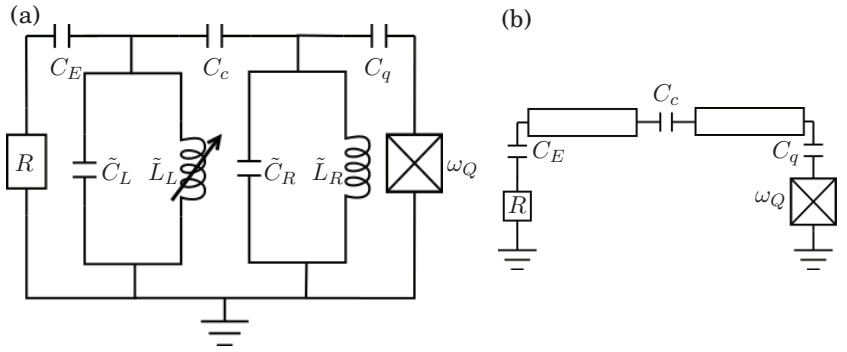

Figure 6.3. (a) The system we consider is comprised of left and right LC oscillators coupled by a capacitance C_c. The right oscillator is weakly coupled by a capacitor C_q, to a transmon qubit, with angular frequency ω_Q, and the left oscillator is coupled via another capacitor C_E, to a resistor which acts as an artificial environment for the qubit. (b) Schematic representation of the setup, which may be used to model a coupled cavity system, in which each resonator represents a single cavity mode. Adapted from Publication IV.

itors, are denoted by $\hat{H}_{C_c}$, $\hat{H}_{C_E}$, and $\hat{H}_{C_q}$, respectively. We take the qubit Hamiltonian $\hat{\tilde{H}}_q$, of a transmon [31, 79, 80] with junction capacitance C_J, Josephson energy E_J, and charging energy E_C. We represent the resistor Hamiltonian, $\hat{\tilde{H}}_r$, as an infinite sum of harmonic oscillators.

We rewrite this Hamiltonian in the more amenable form,

$$\hat{H}_{\text{tot}} = \overbrace{\frac{1}{2}\left(\tilde{C}_L + C_c + C_E\right)\hat{V}_L^2 + \frac{1}{2}L_L\hat{I}_L^2}^{\hat{H}_L} + \overbrace{\frac{1}{2}\left(\tilde{C}_R + C_c + C_q\right)\hat{V}_R^2 + \frac{1}{2}L_R\hat{I}_R^2}^{\hat{H}_R} - \overbrace{C_E\hat{V}_L\delta\hat{V}_r}^{\hat{H}_{\text{int}}} - \overbrace{C_c\hat{V}_L\hat{V}_R}^{\hat{H}_{L-R}} + \overbrace{E_J\cos(\hat{\phi}) + \frac{1}{2}\left(C_J + C_q\right)\hat{V}_q^2}^{\hat{H}_q} - \overbrace{C_q\hat{V}_R\hat{V}_q}^{\hat{H}_{R-q}} + \hat{H}_r. \tag{6.11}$$

That is, in terms of new effective left and right Hamiltonians which retain the form of LC oscillators, but with the modified capacitances, $C_L = \tilde{C}_L + C_c + C_E$, and $C_R = \tilde{C}_R + C_c + C_q$. Equation (3.1) yields the spectrum of $\delta\hat{V}_r$, provided that $\omega \ll 1/(RC_E)$. The effective cavities may be diagonalised by introducing bosonic creation and annihilation operators. Defining $\hat{V}_{L(R)} = V^0_{L(R)}(\hat{a}^\dagger_{L(R)} + \hat{a}_{L(R)})$ where $V^0_{L(R)} = \sqrt{\hbar\omega_{L(R)}/(2C_{L(R)})}$, gives a cavity Hamiltonian $\hat{H}_{L(R)} = \hbar\omega_{L(R)}(\hat{a}^\dagger_{L(R)}\hat{a}_{L(R)} + 1/2)$, with $\omega_{L(R)} = 1/\sqrt{L_{L(R)}C_{L(R)}}$.

We therefore identify the left-right cavity coupling term as $\hat{H}_{L-R} = \hbar\alpha(\hat{a}^\dagger_L\hat{a}^\dagger_R + \hat{a}^\dagger_L\hat{a}_R + \hat{a}_L\hat{a}^\dagger_R + \hat{a}_L\hat{a}_R)$, where we have defined $\alpha = -C_cV^0_LV^0_R/\hbar$. Similarly, with $\hat{b}^{(\dagger)}$ the annihilation (creation) operator for the transmon, taking the voltage over the qubit to be $\hat{V}_q = V^0_q(\hat{b} - \hat{b}^\dagger)$, where $V^0_q =$

$-i\frac{\sqrt{2}e}{C_J+C_q}(\frac{E_J}{8E_C})^{1/4}$ [79], one finds a cavity-qubit coupling $\hat{H}_{R-q} = \hbar g(\hat{b}\hat{a}_R^\dagger + \hat{b}\hat{a}_R - \hat{b}^\dagger\hat{a}_R - \hat{b}^\dagger\hat{a}_R^\dagger)$, with $g = -C_q V_R^0 V_q^0/\hbar$.

We proceed by treating the resistor as an environment for the cavity-qubit system, incorporating the coupling term, $\hat{H}_{\text{int}}$, as a weak perturbation which induces transitions between the cavity-qubit states. This treatment enables us to compute the dynamics of the eigenvector probability distribution from the resulting master equation, as in Eq. (6.9).

We work in the basis $|\sigma, n_L, n_R\rangle$, with $\sigma \in \{g, e\}$, and at low temperatures. We restrict ourselves to the photon number subspace $n_{LR} \in \{0, 1\}$, and hence terms representing simultaneous (de)excitations of photon and/or qubit play no role. In this case, the Hamiltonian may be represented as a 4×4 block diagonal matrix.

$$\hat{H}_{\text{tot}} \hat{=} \hbar \begin{pmatrix} 0 & 0 & 0 & 0 \\ 0 & \omega_L & \alpha & 0 \\ 0 & \alpha & \omega_R & g^* \\ 0 & 0 & g & \omega_Q \end{pmatrix}. \tag{6.12}$$

The general solution for the eigenvectors of the non-trivial 3×3 block are

$$\sin(\theta_k)|g10\rangle + \cos(\theta_k)\sin(\gamma_k)|g01\rangle + \cos(\theta_k)\cos(\gamma_k)|e00\rangle, \tag{6.13}$$

with

$$\gamma_k = \arctan[(\epsilon'_k - \omega_Q)/g], \tag{6.14}$$

$$\theta_k = \arctan\left[\frac{(\epsilon'_k - \omega_Q)}{(\epsilon'_k - \omega_L)} \frac{-i\alpha}{\sqrt{|g|^2 - (\epsilon'_k - \omega_Q)^2}}\right], \tag{6.15}$$

where we have defined $\epsilon'_k = \epsilon_k/\hbar$ using the corresponding eigenvalues ϵ_k. In general, these exact solutions are cumbersome to work with. Nevertheless we can recover useful analytical solutions in several important limits as summarised in Publication IV.

In practice, perhaps the most important of these regimes is the weak coupling limit $\alpha \sim |g| \ll \omega_L, \omega_R, \omega_Q$. We assume that the bare oscillators are non-degenerate, and hence utilize second-order perturbation theory to find the eigenvectors and frequencies $\{|i\rangle, \omega_i\}$. In the far detuned limit these are approximately equivalent to the basis states $|\sigma, n_L, n_R\rangle$ (see Publication IV), and the transition rates between them can be calculated

using Eq. (5.1),

$$\Gamma_{2\to1} = \tilde{A}_2^2 \left(\frac{C_E}{C_L}\right)^2 \left(\frac{2\Delta_{LR}^2 - \alpha^2}{2\omega_{LR}^2}\right)^2 \frac{R\omega_2}{Z_L[1-\exp(\frac{-\hbar\omega_2}{k_B T})]}, \tag{6.16}$$

$$\Gamma_{3\to1} = \tilde{A}_3^2 \left(\frac{C_E}{C_L}\right)^2 \frac{\alpha^2}{\Delta_{RL}^2} \frac{R\omega_3}{Z_L[1-\exp(\frac{-\hbar\omega_3}{k_B T})]}, \tag{6.17}$$

$$\Gamma_{4\to1} = \tilde{A}_4^2 \left(\frac{C_E}{C_L}\right)^2 \frac{|g|^2\alpha^2}{\Delta_{QR}^2\Delta_{QL}^2} \frac{R\omega_4}{Z_L[1-\exp(\frac{-\hbar\omega_4}{k_B T})]}, \tag{6.18}$$

where the $\tilde{A}_i$ are the normalisation constants of the eigenvectors, which are of the order of unity for large detuning. We have also defined $\Delta_{ab} = \omega_b - \omega_a$ in terms of the angular frequencies of the bare oscillators and of the qubit. We observe the deexcitation rate of the state $|4\rangle$ ($\approx |e00\rangle$, if $|\Delta_{QL}|/\alpha, |\Delta_{QR}|/|g| \gg 1$) is proportional to $|g|^2\alpha^2$, that is the excited qubit state is 'doubly protected', firstly by the weak cavity-qubit coupling and secondly by the small coupling of the cavity to the resistor.

Finally, we consider how to select the parameters of the resonator such that the model corresponds to the coupled cavity setup depicted schematically in Fig. 6.3(b)[1]. We assume that the coupling capacitances, and the qubit properties are determined by the geometry of the device, and are therefore equal in both pictures. In order to match the excitation energies, and the voltage operators at the ends of the isolated cavities, we select

$$L_L = \frac{2}{\pi^2} x_c \ell_L, \tag{6.19}$$

$$L_R = \frac{2}{\pi^2} (L - x_c) \ell_R, \tag{6.20}$$

$$\tilde{C}_L = \frac{c x_c}{2}, \tag{6.21}$$

$$\tilde{C}_R = \frac{c(L - x_c)}{2}. \tag{6.22}$$

for the lumped oscillator parameters. Placing a qubit at $x_q = L$ will then give matching spectra in the two models (see Fig. 4.2). Should a qubit offset be desirable, we may define an effective capacitance C_q^{eff}, such that the energy spectra of the two models remain matched. Figure 6.4 presents the dependence C_q^{eff} on the position of the qubit in the right cavity region. In this case, the effective coupling capacitance may be well approximated by $C_q^{\text{eff}} = C_q^0 \cos(2\pi x_q/L)$. By matching the parameters in this way, the lumped element model exhibits similar physical behaviour to the distributed-element model.

[1]With a suitably modified resistor interaction term in the distributed-element model, $\hat{H}_{\text{int}} = C_E \hat{V}_L \otimes \delta\hat{V}_R$. We neglect the effects of C_E, and C_q, when performing the mapping, as these are not included Eq. (4.8).

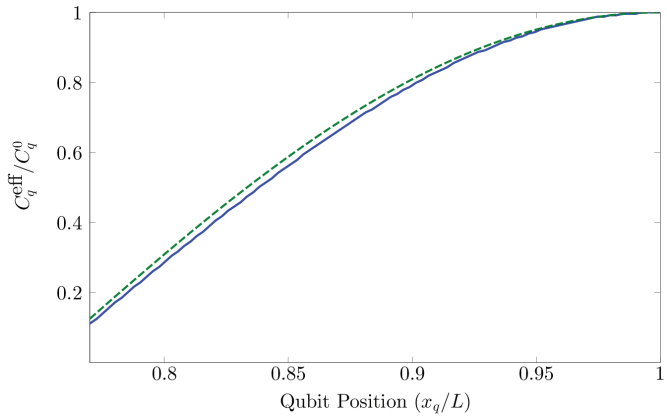

Figure 6.4. Value of the effective coupling capacitance required to match the spectra of the lumped- and distributed-element models as a function of the position of the qubit in the right cavity region. The solid lines gives the numerical solution obtained through matching the low-energy spectra of the two models. The line $C_q^{\text{eff}} = C_q^0 \cos(2\pi x_q/L)$, shown by the dashed line, gives a good approximation to these solutions for $\ell_L = \ell_R$. We use a cavity of length $L = 12$ mm divided into left and right cavities by a capacitance of $C_c = 1$ fF at $x_c = L/2$. The cavity has a capacitance per unit length of $c = 130$ pF, and characteristic impedance $Z_c = 50\ \Omega$. The bare qubit coupling capacitor has a capacitance $C_q^0 = 10$ fF, and the qubit has a frequency of $\omega_Q/(2\pi) = 12.62$ GHz.

7. Summary

This thesis contains theoretical and computational studies of superconducting microwave cavities, embedded with carefully designed normal-metal components. The main goal of the research presented here was to analyse the functionality of these normal-metal components, with the ultimate aim to stimulate experimental activity on expanding the toolbox of circuit quantum electrodynamics by realising the proposed techniques.

To achieve this we approached the topic from two directions, in Publications I and II we showed that a normal-metal island can act as an engineered environment for the cavity and that observation of single-photon heat conduction between two such islands in a cavity was a realistic goal which would open up the possibility of remote heating and refrigeration of cavity components.

Achieving a balance between the competing demands of qubit addressability and coherence time remains an obstacle on the path to engineering a large-scale quantum computer. Publications III and IV suggest a new tool which will potentially contribute in overcoming this challenge. More precisely, we showed that the qubit and photon lifetimes may be tuned independently and *in situ*, allowing for fast system reset, or normal operation as required.

The work here is theoretical but the experimental implications have been considered closely throughout. The experiments are forthcoming, and it will be interesting to see how closely those results match the predictions made here. In the long term, solving the evolution of the full density matrix may be necessary in order to extend the applicability, and account for the interference effects that are not studied in the present approach.

Bibliography

[1] C. E. Shannon, AT&T Tech J. **27**, 379 (1948).

[2] J. S. Bell, Physics **1**, 195 (1964).

[3] A. Aspect, J. Dalibard, and G. Roger, Phys. Rev. Lett. **49**, 1804 (1982).

[4] A. Aspect, Nature (London) **446**, 866 (2007).

[5] R. Landauer, Phys. Lett. A **217**, 188 (1996).

[6] R. Landauer, Physica A **263**, 63 (1999).

[7] S. Lloyd, Phys. Rev. Lett. **88**, 237901 (2002).

[8] R. Landauer, Phys. Today **44**, 23 (1991).

[9] A. Barenco, Contemp. Phys. **37**, 375 (1996).

[10] A. Steane, Rep. Prog. Phys. **61**, 117 (1998).

[11] T. D. Ladd, F. Jelezko, R. Laflamme, Y. Nakamura, C. Monroe, and J. L. O'Brien, Nature (London) **464**, 45 (2010).

[12] J. Cirac and P. Zoller, Nature (London) **404**, 579 (2000).

[13] V. Cerletti, W. Coish, O. Gywat, and D. Loss, Nanotechnology **16**, R27 (2005).

[14] P. Kok, W. J. Munro, K. Nemoto, T. C. Ralph, J. P. Dowling, and G. J. Milburn, Rev. Mod. Phys. **79**, 135 (2007).

[15] D. DiVincenzo, Fortschr. Phys. **48**, 771 (2000).

[16] L. Vandersypen, M. Steffen, G. Breyta, C. Yannoni, M. Sherwood, and I. Chuang, Nature (London) **414**, 883 (2001).

[17] E. Martin-Lopez, A. Laing, T. Lawson, R. Alvarez, X.-Q. Zhou, and J. L. O'Brien, Nature Photon. **6**, 773 (2012).

[18] A. Ekert and R. Jozsa, Rev. Mod. Phys. **68**, 733 (1996).

[19] S. Beauregard, Quant. Inf. Comput. **3**, 175 (2003).

[20] A. M. Steane, Nature (London) **399**, 124 (1999).

[21] B. P. Lanyon, J. D. Whitfield, G. G. Gillett, M. E. Goggin, M. P. Almeida, I. Kassal, J. D. Biamonte, M. Mohseni, B. J. Powell, M. Barbieri, A. Aspuru-Guzik, and A. G. White, Nature Chem. **2**, 106 (2010).

[22] D. S. Abrams and S. Lloyd, Phys. Rev. Lett. **83**, 5162 (1999).

[23] A. J. Leggett, Prog. Theor. Phys. Supp. **69**, 80 (1980).

[24] Y. Nakamura, Y. Pashkin, and J. Tsai, Nature (London) **398**, 786 (1999).

[25] J. Friedman, V. Patel, W. Chen, S. Tolpygo, and J. Lukens, Nature (London) **406**, 43 (2000).

[26] I. Chiorescu, Y. Nakamura, C. J. P. M. Harmans, and J. E. Mooij, Science **299**, 1869 (2003).

[27] Y. Makhlin and A. Shnirman, Phys. Rev. Lett. **92**, 178301 (2004).

[28] Y. Pashkin, O. Astafiev, T. Yamamoto, Y. Nakamura, and J. Tsai, Quant. Inf. Proc. **8**, 55 (2009).

[29] H. Paik, D. I. Schuster, L. S. Bishop, G. Kirchmair, G. Catelani, A. P. Sears, B. R. Johnson, M. J. Reagor, L. Frunzio, L. I. Glazman, S. M. Girvin, M. H. Devoret, and R. J. Schoelkopf, Phys. Rev. Lett. **107**, 240501 (2011).

[30] G. Ithier, E. Collin, P. Joyez, P. Meeson, D. Vion, D. Esteve, F. Chiarello, A. Shnirman, Y. Makhlin, J. Schriefl, and G. Schon, Phys. Rev. B **72**, 134519 (2005).

[31] J. A. Schreier, A. A. Houck, J. Koch, D. I. Schuster, B. R. Johnson, J. M. Chow, J. M. Gambetta, J. Majer, L. Frunzio, M. H. Devoret, S. M. Girvin, and R. J. Schoelkopf, Phys. Rev. B **77**, 180502 (2008).

[32] J. Martinis, S. Nam, J. Aumentado, K. Lang, and C. Urbina, Phys. Rev. B **67**, 094510 (2003).

[33] J. Clarke and F. K. Wilhelm, Nature (London) **453**, 1031 (2008).

[34] I. Siddiqi, Supercond. Sci. Technol. **24**, 091002 (2011).

[35] A. Megrant, C. Neill, R. Barends, B. Chiaro, Y. Chen, L. Feigl, J. Kelly, E. Lucero, M. Mariantoni, P. J. J. O'Malley, D. Sank, A. Vainsencher, J. Wenner, T. C. White, Y. Yin, J. Zhao, et al., App. Phys. Lett. **100**, 113510 (2012).

[36] A. Blais, R. S. Huang, A. Wallraff, S. M. Girvin, and R. J. Schoelkopf, Phys. Rev. A **69**, 062320 (2004).

[37] A. Wallraff, D. I. Schuster, A. Blais, L. Frunzio, R. S. Huang, J. Majer, S. Kumar, S. M. Girvin, and R. J. Schoelkopf, Nature (London) **431**, 162 (2004).

[38] A. Blais, J. Gambetta, A. Wallraff, D. I. Schuster, S. M. Girvin, M. H. Devoret, and R. J. Schoelkopf, Phys. Rev. A. **75**, 032329 (2007).

[39] J. M. Fink, M. Goeppl, M. Baur, R. Bianchetti, P. J. Leek, A. Blais, and A. Wallraff, Nature (London) **454**, 315 (2008).

[40] M. Mariantoni, H. Wang, R. C. Bialczak, M. Lenander, E. Lucero, M. Neeley, A. D. O'Connell, D. Sank, M. Weides, J. Wenner, T. Yamamoto, Y. Yin, J. Zhao, J. M. Martinis, and A. N. Cleland, Nature Phys. **7**, 287 (2011).

[41] T. Niemczyk, F. Deppe, H. Huebl, E. P. Menzel, F. Hocke, M. J. Schwarz, J. J. Garcia-Ripoll, D. Zueco, T. Huemmer, E. Solano, A. Marx, and R. Gross, Nature Phys. **6**, 772 (2010).

[42] T. Yamamoto, Y. Pashkin, O. Astafiev, Y. Nakamura, and J. Tsai, Nature (London) **425**, 941 (2003).

[43] J. Majer, J. M. Chow, J. M. Gambetta, J. Koch, B. R. Johnson, J. A. Schreier, L. Frunzio, D. I. Schuster, A. A. Houck, A. Wallraff, A. Blais, M. H. Devoret, S. M. Girvin, and R. J. Schoelkopf, Nature (London) **449**, 443 (2007).

[44] M. A. Sillanpää, J. I. Park, and R. W. Simmonds, Nature (London) **449**, 438 (2007).

[45] M. Steffen, M. Ansmann, R. C. Bialczak, N. Katz, E. Lucero, R. McDermott, M. Neeley, E. M. Weig, A. N. Cleland, and J. M. Martinis, Science **313**, 1423 (2006).

[46] M. Ansmann, H. Wang, R. C. Bialczak, M. Hofheinz, E. Lucero, M. Neeley, A. D. O'Connell, D. Sank, M. Weides, J. Wenner, A. N. Cleland, and J. M. Martinis, Nature (London) **461**, 504 (2009).

[47] L. DiCarlo, M. D. Reed, L. Sun, B. R. Johnson, J. M. Chow, J. M. Gambetta, L. Frunzio, S. M. Girvin, M. H. Devoret, and R. J. Schoelkopf, Nature (London) **467**, 574 (2010).

[48] L. DiCarlo, J. M. Chow, J. M. Gambetta, L. S. Bishop, B. R. Johnson, D. I. Schuster, J. Majer, A. Blais, L. Frunzio, S. M. Girvin, and R. J. Schoelkopf, Nature (London) **460**, 240 (2009).

[49] E. Lucero, R. Barends, Y. Chen, J. Kelly, M. Mariantoni, A. Megrant, P. O'Malley, D. Sank, A. Vainsencher, J. Wenner, T. White, Y. Yin, A. N. Cleland, and J. M. Martinis, Nature Phys. **8**, 719 (2012).

[50] A. A. Houck, D. I. Schuster, J. M. Gambetta, J. A. Schreier, B. R. Johnson, J. M. Chow, L. Frunzio, J. Majer, M. H. Devoret, S. M. Girvin, and R. J. Schoelkopf, Nature (London) **449**, 328 (2007).

[51] D. I. Schuster, A. A. Houck, J. A. Schreier, A. Wallraff, J. M. Gambetta, A. Blais, L. Frunzio, J. Majer, B. Johnson, M. H. Devoret, S. M. Girvin, and R. J. Schoelkopf, Nature (London) **445**, 515 (2007).

[52] D. Bozyigit, C. Lang, L. Steffen, J. M. Fink, C. Eichler, M. Baur, R. Bianchetti, P. J. Leek, S. Filipp, M. P. da Silva, A. Blais, and A. Wallraff, Nature Phys. **7**, 154 (2011).

[53] E. Zakka-Bajjani, F. Nguyen, M. Lee, L. R. Vale, R. Simmonds, and J. Aumentado, Nature Phys. **7**, 599 (2011).

[54] M. Hofheinz, H. Wang, M. Ansmann, R. C. Bialczak, E. Lucero, M. Neeley, A. D. O'Connell, D. Sank, J. Wenner, J. M. Martinis, and A. N. Cleland, Nature (London) **459**, 546 (2009).

[55] A. Palacios-Laloy, F. Nguyen, F. Mallet, P. Bertet, D. Vion, and D. Esteve, J. Low Temp. Phys. **151**, 1034 (2008).

[56] M. Sandberg, C. M. Wilson, F. Persson, T. Bauch, G. Johansson, V. Shumeiko, T. Duty, and P. Delsing, App. Phys. Lett. **92** (2008).

[57] J. M. Gambetta, A. A. Houck, and A. Blais, Phys. Rev. Lett. **106**, 030502 (2011).

[58] S. J. Srinivasan, A. J. Hoffman, J. M. Gambetta, and A. A. Houck, Phys. Rev. Lett. **106**, 083601 (2011).

[59] C. M. Wilson, G. Johansson, A. Pourkabirian, M. Simoen, J. R. Johansson, T. Duty, F. Nori, and P. Delsing, Nature (London) **479**, 376 (2011).

[60] P. Lähteenmäki, G. S. Paraoanu, J. Hassel, and P. J. Hakonen, Proc. Natl. Acad. Sci. U.S.A. **110**, 4234 (2013).

[61] J. Pendry, J. Phys.: Condens. Matter **11**, 6621 (1999).

[62] L. G. C. Rego and G. Kirczenow, Phys. Rev. Lett. **81**, 232 (1998).

[63] O. Chiatti, J. T. Nicholls, Y. Y. Proskuryakov, N. Lumpkin, I. Farrer, and D. A. Ritchie, Phys. Rev. Lett. **97**, 056601 (2006).

[64] K. Schwab, E. Henriksen, J. Worlock, and M. Roukes, Nature (London) **404**, 974 (2000).

[65] M. Meschke, W. Guichard, and J. P. Pekola, Nature (London) **444**, 187 (2006).

[66] D. R. Schmidt, R. J. Schoelkopf, and A. N. Cleland, Phys. Rev. Lett. **93**, 045901 (2004).

[67] A. V. Timofeev, M. Helle, M. Meschke, M. Möttönen, and J. P. Pekola, Phys. Rev. Lett. **102**, 200801 (2009).

[68] A. A. Clerk, M. H. Devoret, S. M. Girvin, F. Marquardt, and R. J. Schoelkopf, Rev. Mod. Phys. **82**, 1155 (2010).

[69] T. Ruokola and T. Ojanen, Phys. Rev. B **86**, 035454 (2012).

[70] L. M. A. Pascal, H. Courtois, and F. W. J. Hekking, Phys. Rev. B **83**, 125113 (2011).

[71] J. T. Muhonen, M. Meschke, and J. P. Pekola, Rep. Prog. Phys. **75**, 046501 (2012).

[72] F. Giazotto, T. T. Heikkilä, A. Luukanen, A. M. Savin, and J. P. Pekola, Rev. Mod. Phys. **78**, 217 (2006).

[73] J. Pekola, J. Low Temp. Phys. **135**, 723 (2004).

[74] S. Kafanov, A. Kemppinen, Y. A. Pashkin, M. Meschke, J. S. Tsai, and J. P. Pekola, Phys. Rev. Lett. **103**, 120801 (2009).

[75] P. J. Koppinen and I. J. Maasilta, Phys. Rev. Lett. **102**, 165502 (2009).

[76] D. Pozar, *Microwave Engineering* (Wiley, Hoboken, 2004).

[77] A. O. Caldeira and A. J. Leggett, Phys. Rev. Lett. **46**, 211 (1981).

[78] D. F. Walls and G. J. Milburn, *Quantum Optics 2nd Edition* (Springer, Berlin, 2008).

[79] J. Koch, T. M. Yu, J. Gambetta, A. A. Houck, D. I. Schuster, J. Majer, A. Blais, M. H. Devoret, S. M. Girvin, and R. J. Schoelkopf, Phys. Rev. A **76**, 042319 (2007).

[80] A. A. Houck, J. Koch, M. H. Devoret, S. M. Girvin, and R. J. Schoelkopf, Quant. Inf. Proc. **8**, 105 (2009).

Publication I

Philip Jones, Jukka Huhtamäki, Kuan Yen Tan, and Mikko Möttönen. Single-photon heat conduction in electrical circuits. *Physical Review B*, 85, 075413, February 2012.

Errata

This paper contains the following errors, which have a minor effect on the stated results.

1. The effective resistance in Eq. (3) was defined as $R_{\text{eff}}^{(i)} = R_i \sin(\pi x_i / L)$, which is correct only for the first mode. In general, the effective resistance is a function of the mode number, $R_{\text{eff}}^{(i,k)} = R_i \sin(k\pi x_i / L)$. This was handled correctly in the simulations, and hence has no effect on the numerical results.

2. The value for the coupling strength γ was given as 1.53×10^9 s^{-1}, rather than 1.46×10^{10} s^{-1}. This error was propagated to the estimate of the Q-value, which was a factor of 10 too large as a result. The saturation temperatures for the parameters used in the paper are therefore likely to be slightly optimistic in comparison to what is realistically achievable in practice. Nevertheless, this error has no effect on the essential features of the results, and all of the conclusions remain perfectly valid. Note that this error is not present in the analysis or simulations of Chapter 5.

Aalto-DD 104/2013

ISBN 978-952-60-5224-3
ISBN 978-952-60-5225-0 (pdf)
ISSN-L 1799-4934
ISSN 1799-4934
ISSN 1799-4942 (pdf)

Aalto University
School of Science
Department of Applied Physics
www.aalto.fi

BUSINESS +
ECONOMY

ART +
DESIGN +
ARCHITECTURE

SCIENCE +
TECHNOLOGY

CROSSOVER

**DOCTORAL
DISSERTATIONS**